We are IntechOpen, the world's leading publisher of Open Access books Built by scientists, for scientists

4,800
Open access books available

122,000
International authors and editors

135M
Downloads

Our authors are among the

154
Countries delivered to

TOP 1%
most cited scientists

12.2%
Contributors from top 500 universities

WEB OF SCIENCE™

Selection of our books indexed in the Book Citation Index in Web of Science™ Core Collection (BKCI)

Interested in publishing with us?
Contact book.department@intechopen.com

Numbers displayed above are based on latest data collected.
For more information visit www.intechopen.com

Chapter 2

Land-Atmosphere Interaction in the Southwestern Karst Region of China

Jiangbo Gao, Wenjuan Hou, Kewei Jiao and Shaohong Wu

Additional information is available at the end of the chapter

http://dx.doi.org/10.5772/64740

Abstract

Land-atmosphere interaction in the southwestern Karst region of China was investigated from two aspects: response of land cover to climate change and climatic effects of Karst rocky desertification. The first part focused on the temporal-spatial variation of growing-season normalized difference vegetation index (NDVI) and its relationship with climate variables. The relationships between growing-season NDVI with temperature and precipitation were both positive, indicating its limiting role on the distribution and dynamic of vegetation cover in the study area. The second part was designed to investigate whether the changed vegetation cover and land surface processes in the Karst regions was capable of modifying the summer climate simulation over East Asia. It was shown that land desertification resulted in the reduced net radiation and evaporation in the degraded areas. The East Asian summer monsoon was weakened after land degradation. Such circulation differences favored the increase in moisture flux and clouds, and thereby causing more precipitation in southeast coastal areas. Based on the above findings, it can be concluded that vegetation cover in Karst region was sensitive to climate change at larger scale, and on the other hand, there was significant feedback of vegetation cover change to regional climate by altering water and energy balance.

Keywords: Karst rocky desertification, climate change, land cover, southwest China, land-atmosphere interaction

1. Introduction

During the past decades, the vegetation-climate interaction has been a research focus of meteorology, climatology, geography, and ecology. The contents mainly include the impact of climate change on ecosystem and the feedback of vegetation cover change to atmosphere. Investigation on the correlation between vegetation variation and climate change and its influencing mechanisms are the basis for the studies on climate change adaptation and mitigation.

The response of terrestrial ecosystem to climate change, a complex issue in the field of global change, has been focused on in the last 30 years [1]. Vegetation cover has been proven to be governed by climatic factors, such as precipitation, temperature, solar radiation, and CO_2 concentration. Therefore, variation in vegetation and its relationship with climatic factors reflected the sensitivity and vulnerability of the ecosystem to climate change (i.e., the responding processes) [2]. In many studies, the normalized difference vegetation index (NDVI) was selected to detect the impact of climate change on vegetation activity in Eurasia, [3–5]. Although the temperature increase was detected to dominate the vegetation cover and its dynamic in the northwestern China, western China, and the Tibetan Plateau, the impact of precipitation in the arid and semiarid regions may be more significant. The complicated and spatial heterogeneous effects of climate change on NDVI indicate the need to conduct further investigation at regional scales. Recently, in order to make clear the role of vegetation cover in the regional climate change, several studies on the feedback of land cover to atmosphere were conducted, especially after 1990s [6]. Land cover change (LCC) was documented as important as atmospheric circulation and solar orbit perturbations in climate change [7]. On the other hand, the feedback is regional-dependent due to the complicated climate and LCC in different regions.

The Karst region in the southwest China presents the transformation from vegetation covered landscape to exposed basement rocks, which was defined as the Karst rock desertification (KRD). In this region, the natural ecosystem is vulnerable while the human disturbance is severe. Earlier studies mainly emphasized the impact of land use change on vegetation cover [8–10], lacking consideration of climate change impacts at large scales. Furthermore, it is unknown the climatic effects of land cover change in the Karst region, especially land degradation. Therefore, in this chapter, the southwestern Karst region of China was selected to conduct land-atmosphere interactions research.

2. Study area

The southwestern Karst region of China, at 101°73'–112°44'E and 21°26'–29°25'N, and the Guizhou Karst Plateau, in the center of the southwestern Karst region (**Figure 1**), were selected to conduct research of climatic impacts on vegetation cover and climatic effects of vegetation degradation, respectively. They are located in the subtropical/tropical monsoon climate zone with annual precipitation of above 900 mm. The temperature and precipitation present great

http://dx.doi.org/10.5772/64740

difference in spatial patterns, because of the typical topographical features with widely distributed mountains. Besides the Guizhou Karst Plateau, the southwestern Karst region, approximately 5.5×10^6 km^2, includes Guangxi Zhuang Autonomous Region (GX) and eastern part of Yunnan Province (YN).

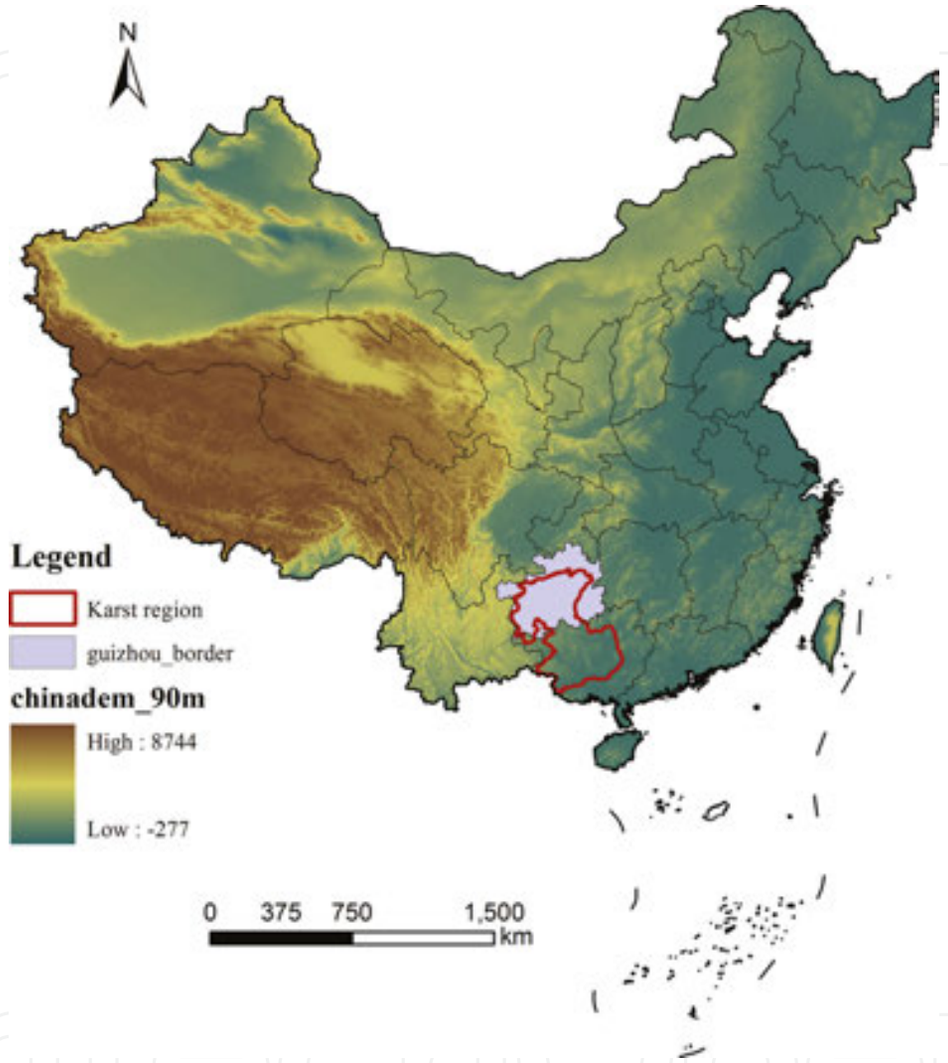

Figure 1. Location of the southwestern Karst region of China and the Guizhou Province of China.

There are six vegetation types in the study area, including broadleaf forest, coniferous forest, shrub, grass, meadow, and cultural vegetation, with shrub covering the largest area. Because of the widely distributing bare limestone and the unsuitable land use since 1950s, KRD covers over 20% of the total area with the desertification rate of 2.5×10^4 km^2 per year, and thus has become the most serious environmental problem in the study area. Rocky desertification in GKP exhibits three characteristics of severe degree, large area and high risk. However, litter research was carried out to assess the long-term vegetation dynamics and its influence on regional climate change.

3. Materials and methods

3.1. Statistical methods

3.1.1. Trend analysis

The NDVI trend from 1982 to 2013 at pixel scale was estimated using the ordinary least squares (OLS) based on the ArcGIS 10.1 platform:

$$\theta_{slope} = \frac{n \times \sum_{i=1}^{n} i \times NDVI - \sum_{i=1}^{n} i \sum_{i=1}^{n} NDVI_i}{n \times \sum_{i=1}^{n} i^2 - \left(\sum_{i=1}^{n} i \right)^2} \quad (1)$$

where θ is the regression slope and n represents the study year during the research period. The positive value of θ means increasing NDVI.

3.1.2. Mann-Kendall ***(MK) test***

Mann-Kendall analysis, applied as a nonparametric, rank-based method for evaluating trends in time-series data [11], was used to detect the changing trend because it is known as more resilient to outliers. A rank sequence (S_k) for time series was built:

$$S_K = \sum_{i=1}^{k} r_{i(k=2,3,\ldots,n)} \quad (2)$$

where k is the dataset record length over years, and r_i is the altered data series for original dataset:

$$r_i = \begin{pmatrix} 1 & x_i > x_j \\ 0 & x_i < x_j \end{pmatrix}_{(j=1,2,\ldots,i)} \quad (3)$$

Under the assumption of random and independent time series, the statistic Z is defined:

$$Z_k = \frac{[S_k - E(S_k)]}{\sqrt{Var(S_k)}} (k = 1,2,\ldots,n) \quad (4)$$

Moreover, $Z_1 = 0$, $E(S_k)$ and Var (S_k) is the mathematical expectation and variance, respectively:

$$E(S_k) = \frac{n(n-1)}{4} \tag{5}$$

$$Var(S_k) = \frac{n(n-1)(2n+5)}{72} \tag{6}$$

The positive Z_k value means the trend is increasing. Compared Z_k with Z_α, the result of $|Z_k| > Z_\alpha$ ($Z0.05 = 1.96$) means the trend is statistically significant.

3.1.3. Ordinary linear square

In order to compare the relative importance of temperature and precipitation for NDVI, the multivariate regression and the standardized coefficients were applied together. The higher standardized values mean important roles. The MATLAB 8.1 was used to establish multivariate linear model:

$$NDVI = b_0 + b_1 \times Temperature + b_2 \times \Pr ecipitation + \varepsilon \tag{7}$$

where b_0, b_1, and b_2 are the regression parameters, while ε is the regression residual. Because of the different range for values of temperature and precipitation, it required normalization to compare the relative importance of climatic factors in the NDVI variations:

$$b_i^{'} = b_i \times \sqrt{\frac{\sum_{t=1}^{n}\left(x_t - \bar{x}\right)}{\sum_{t=1}^{n}\left(y_t - \bar{y}\right)}} \tag{8}$$

3.1.4. Geographically weighted regression (GWR)

The GWR analysis, coupled in ArcGIS 10.1, was conducted to reveal the spatial variations in relationships between NDVI and climatic variables. Both the spatial distribution and the dynamics of NDVI were considered by the GWR model. GWR extends the traditional OLS to consider the spatial heterogeneity in climate-vegetation correlations by assigning weight values [12]:

$$y_i = \beta_0(\mu_i, \nu_i) + \sum_{k=1}^{p} \beta_k(\mu_i, \nu_i) x_{ik} + \varepsilon_i \tag{9}$$

where y_i, x_{ik}, and ε_i, represent the dependent variable, the independent variables, and the random error term at location i, respectively. Note that (μ_i, ν_i) expresses the coordinate location of the ith point, k denotes the independent variable number. β_0 and β_k are the regression parameters at location i.

The regression coefficients were estimated by:

$$\beta(\mu_i,\nu_i) = (X^T W(\mu_i,\nu_i)X)^{-1} X^T W(\mu_i,\nu_i)Y \tag{10}$$

β is the unbiased estimate of the regression coefficient. W is the weighting matrix, and X and Y are matrices for independent and dependent variables, respectively. The kernel function, used to determine the weight, was performed as the exponential distance decay:

$$\omega_{ij} = \exp = \left(\frac{d_{ij}^2}{b^2}\right) \tag{11}$$

ω_{ij} expresses the weight of observation j for location i, d_{ij} represents the Euclidean distance between points i and j, and b is the kernel bandwidth.

3.2. WRF climate model and experimental design

The WRF-ARW was developed as the next generation for regional climate model. It includes different parameterization schemes for longwave and shortwave radiation, cloud microphysics, cumulus, and land surface processes. The simplified simple biosphere model (SSiB), coupled with WRF model, was selected to simulate land surface energy balance. According to the SSiB model description, there are 12 types of vegetation cover, while the vegetation and soil parameters were set for every types. Defining different vegetation cover types in this study enabled investigation of the impact of land degradation and Karst rocky desertification using the WRF-SSiB model. The domain for WRF model was set as follows: dimensions of 196 × 154 horizontal grid points with center at 35°N and 110°E. In this domain, the influencing factors for East Asian summer monsoon can be included, for example, the upper level westerly jet (ULJ) and low-level jet (LLJ), the Bay of Bengal and the southeast trade wind, and so on [13]. The WRF downscaling ability was assessed by comparing the simulations with different physical schemes (**Table 1**), and the optimal combination was concluded from the assessment. For the execution of the WRF, we used the NCEP DOE Reanalysis-2 [14], hereafter NCEP R-2, at 6-h intervals to provide initial conditions and lateral boundary conditions.

Two experiments were done. One was the Case C, using the original SSiB vegetation map (as shown in **Figure 2a**), the other was Case D with the degraded land cover types (**Figure 2b**). The degraded types were decided based on the spatial pattern of different rocky desertification degrees [15]. For example, if the deserted areas accounted more than 30% of the corresponding counties, the SSiB vegetation was modified to bare soil (type 11 in SSiB model). The type 9

(broadleaf shrubs with bare soil) was used to replace original vegetation types in areas described as desert and potential desert areas larger than 45% of the counties and smaller than 30% of the counties, respectively. Based on the reset of vegetation cover types, two vegetation maps were used in WRF model, and was further used to conduct Case C and Case D.

Cases	Microphysics	Long-wave radiation	Short-wave radiation	Factors	R	Bias	RMSE
1	WSM 3	RRTM	MM5(Dudhia)	Precipitation	0.70	1.68	4.07
				Temperature	0.89	3.48	4.65
2	Kessler	RRTM	MM5(Dudhia)	Precipitation	0.37	1.02	5.50
3	Purdue Lin	RRTM	MM5(Dudhia)	Precipitation	0.65	2.64	6.28
4	WSM5	RRTM	MM5(Dudhia)	Precipitation	0.67	2.84	6.58
5	Ferrier	RRTM	MM5(Dudhia)	Precipitation	0.66	2.81	6.30
6	WSM 3	CAM	CAM	Precipitation	0.65	1.91	4.33
				Temperature	0.88	2.97	4.08
7	WSM 3	RRTMG	RRTMG	Precipitation	0.67	3.04	5.41
				Temperature	0.89	2.24	3.65

R, correlation coefficient; RMSE: root mean square error.

Table 1. Descriptive statistics of precipitation and temperature from WRF/SSiB with different microphysics and radiation schemes for June 2000 over 18°-52°N, 86°-136°E.

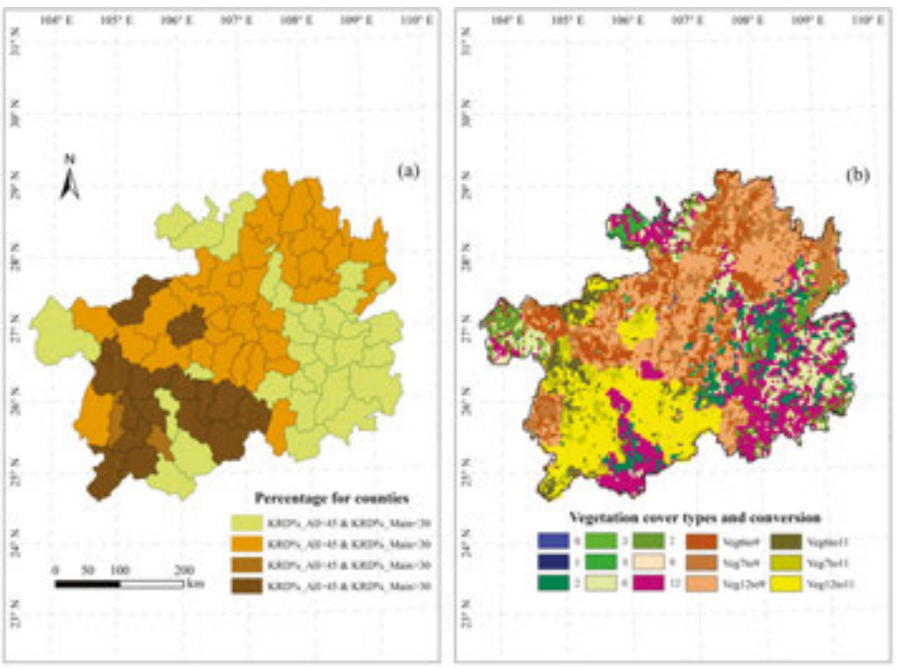

Figure 2. Potential LCC based on the spatial pattern of KRD in GKP. (a) The percentage of areas with KRD for counties. (b) SSiB vegetation map for GKP and vegetation cover conversion.

4. Results and discussion

4.1. Variations in growing-season NDVI

As shown in **Figure 3**, the rate of 0.0015/year during 1982–2013 was estimated for the growing-season NDVI trend in the Karst region of southwest China. The maximum value can be found in 2009 with significant variations between different years. It is indicated in **Figure 3(b)** that the year of 1994 was a tipping point, which means that there were two states before and after this year for the NDVI anomaly. We observed decreasing trend for some years, although the overall trend was increasing. Furthermore, the M-K trend test showed significant increasing trend, especially after the year 2004. As for the variation in NDVI of different vegetation types, the increasing rate was highest for coniferous forest, and the smallest value for meadow (**Table 2**).

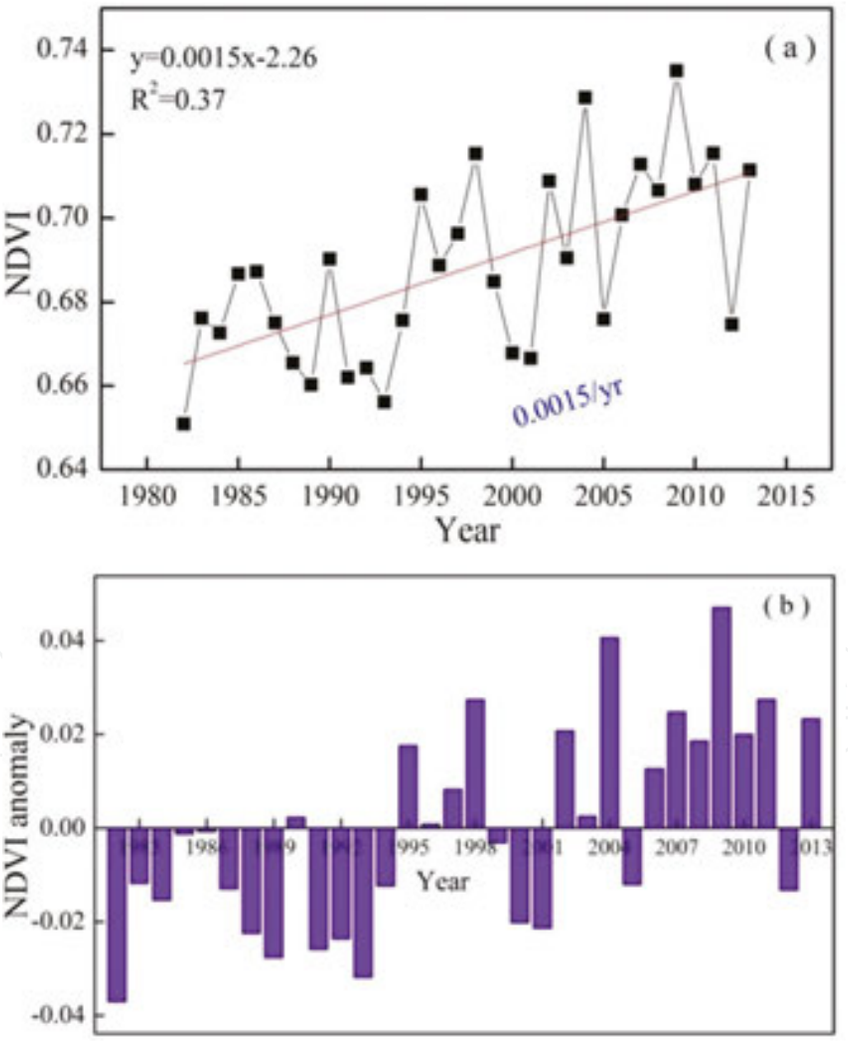

Figure 3. Interannual variations in growing-season NDVI (a) and NDVI anomaly (b) during 1982-2013 in the entire region, using the annual average growing-season NDVI.

http://dx.doi.org/10.5772/64740

Vegetation type	Growing-season NDVI value			NDVI rate	Correlation coefficients	
	Average	Maximum	Minimum		Temperature	Precipitation
Broadleaf forest	0.7412	0.8501	0.5056	0.0013	0.315**	0.173**
Shrub	0.6952	0.8369	0.4866	0.0015	0.149**	0.130**
Grassland	0.6946	0.8405	0.4126	0.0013	0.493**	0.289**
Coniferous forest	0.6871	0.8270	0.3932	0.0016	0.252**	0.063
Cultural vegetation	0.6706	0.8398	0.3576	0.0015	0.374**	0.182**
Meadow	0.5910	0.7319	0.4741	0.0008	0.412**	−0.109

**means a 0.01 significance level.

Table 2. Statistical characteristics of growing-season NDVI for different vegetation types during 1982–2013.

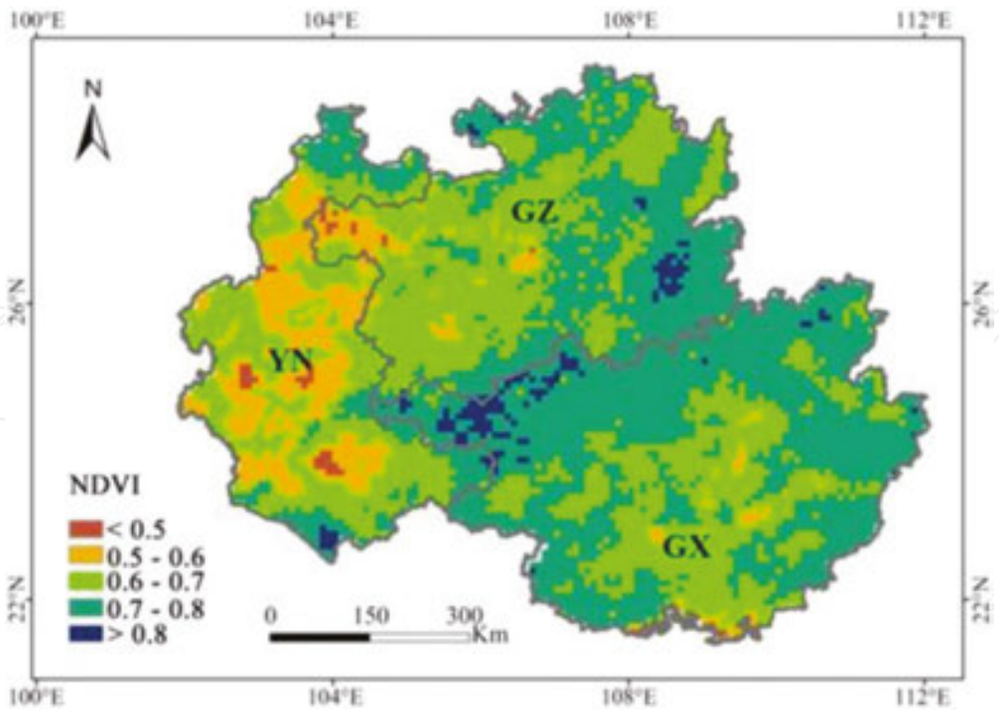

Figure 4. Spatial patterns of average values in growing-season NDVI during 1982–2013.

Figure 4 shows the spatial distribution of NDVI values in the study area, ranging from 0.32 to 0.85. Due to higher temperature and more precipitation in Guangxi Zhuang Autonomous Region, there were high values of NDVI in the east part of the study area. Under the background of complex climate change, there was also spatial heterogeneity for the dynamical variation of NDVI. The higher increasing rate was observed in the northwest and the smaller values in the southeast (**Figure 5**).

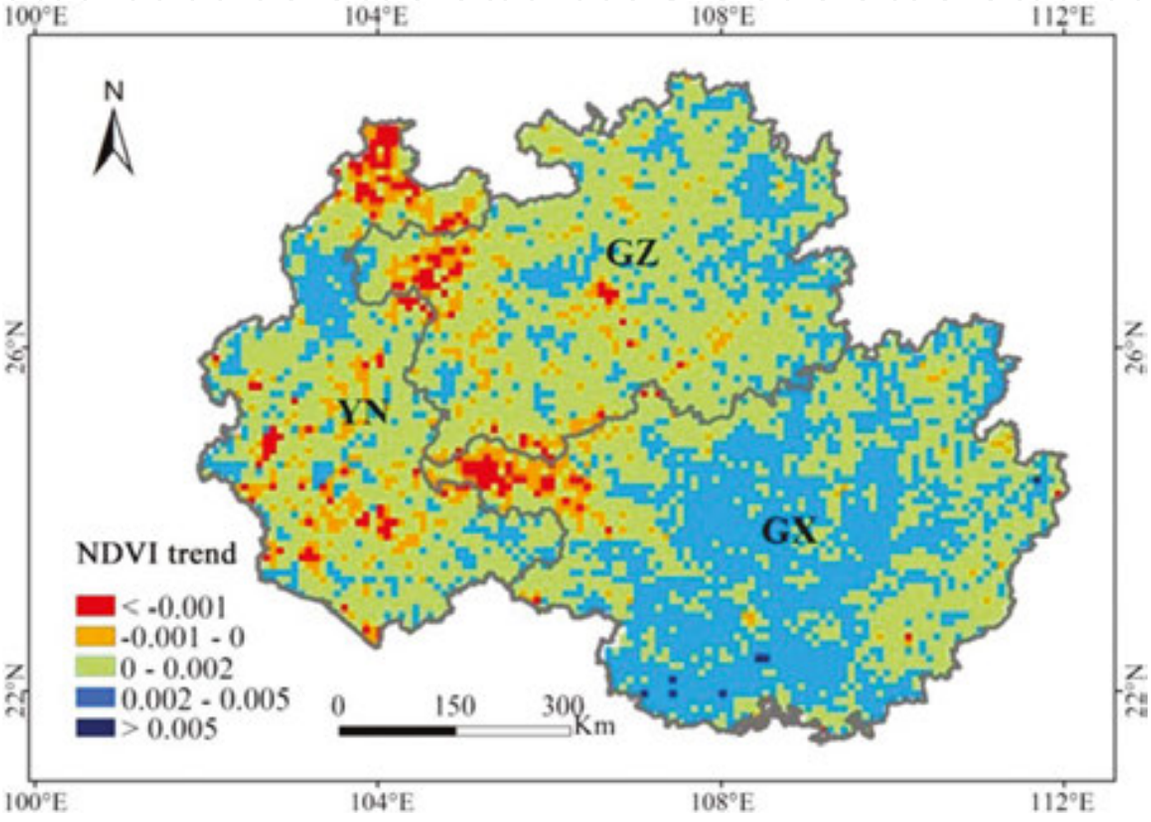

Figure 5. Spatial patterns of temporal trend in growing-season NDVI during 1982–2013.

4.2. Correlations between NDVI and climate factors

We observed warming rate of 0.018°C/year in the study area (**Figure 6a**). It fluctuated from −0.6 ~ 0.8°C for average growing-season temperature. The year of 1995 was a tipping point for temperature and NDVI changes. Specifically, the average temperature for different months presented obvious variations with a maximum temperature (25.2°C) in July. For the changes in precipitation, **Figure 6(c)** shows a decrease of −1.21mm/year during 1982–2013. The dynamic processes for precipitation can be classified as falling under three stages: 1982–1992, 1993–2002, and 2003–2013 (**Figure 6d**). Additionally, the significant uptrend for temperature can be concluded from the Mann-Kendall test.

http://dx.doi.org/10.5772/64740

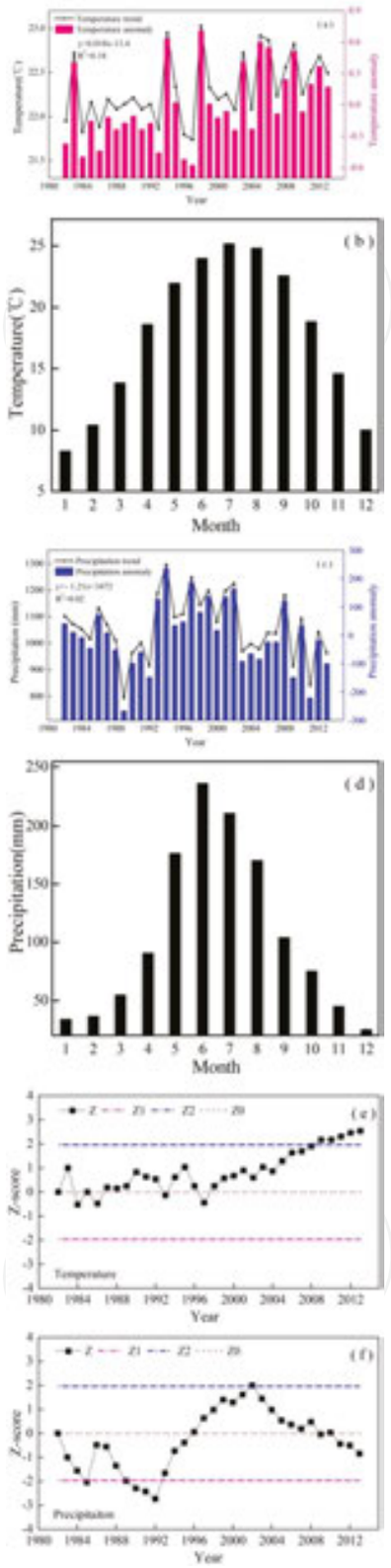

Figure 6. Interannual variations in average growing-season temperature trend and anomaly (**a**); monthly temperature (**b**); precipitation trend and anomaly (**c**); monthly precipitation (**d**); and the results (**e**, **f**) of Mann-Kendall test during 1982–2013 in the entire region.

4.2.1. Traditional linear regression for NDVI and climate variables

As shown in **Figure 7(a)**, there was obvious synergy for NDVI and temperature, but the synergy for NDVI and precipitation was relatively weak (**Figure 7b**). The lower regression coefficients of precipitation indicated the weaker impact of precipitation on vegetation cover change. The reason may be that there was rich rainfall in the study area, and the annual variation cannot play significant roles. Moreover, the correlations between NDVI and climatic variables were different for different vegetation types (shown in **Table 2**). The largest regression coefficient was in grassland.

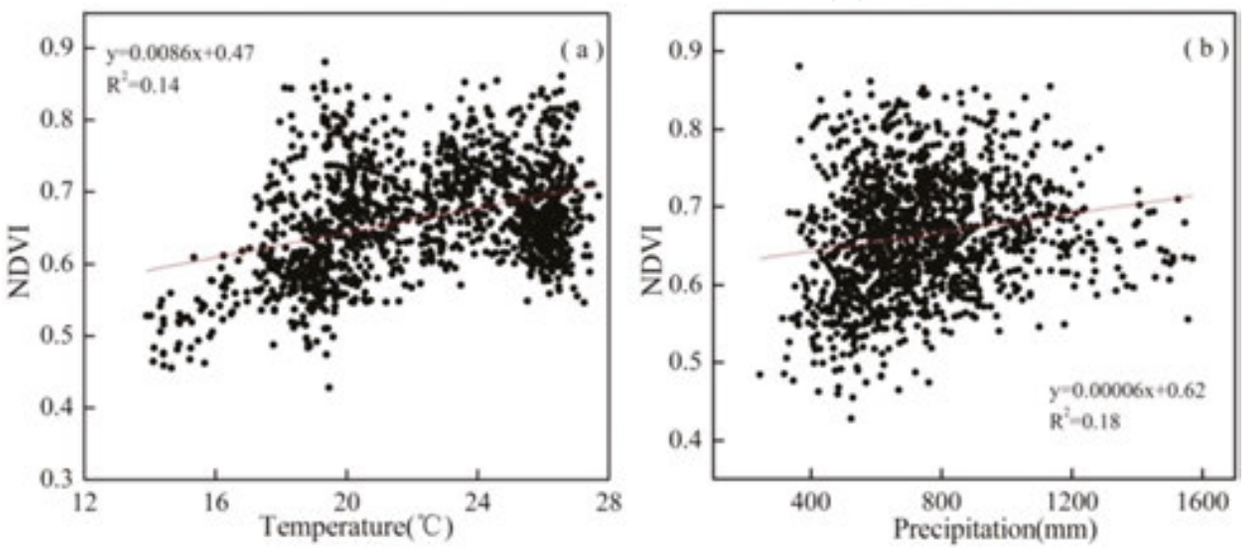

Figure 7. The overall relationship between annual growing-season NDVI and temperature (**a**); precipitation (**b**) during 1982–2013.

In most areas, the relationship between NDVI and temperature (**Figure 8a**) was positive due to the strengthened photosynthesis and vegetation activity by the increase in temperature. It should be pointed out that only within an appropriate range, the temperature rise can result in beneficial effects, and if the temperature is too high, it will cause negative impact on vegetation growth. **Figure 8(b)** shows the regression coefficient for NDVI and precipitation. Although the correlation was positive in most of the areas, there were some negative values in the northern part of the study area.

4.2.2. Local regression for the spatial relationships

The later one means applying the changing rate of NDVI (**Figure 5**) as the dependent variable of GWR while the changing rate of climatic factors as independent variables. **Figure 9** lists the GWR regression coefficients, where colors ranging from blue to red represented values from low to high. Additionally, the standard errors were analyzed by the points with different sizes.

There was positive relationships between multiyear average NDVI and temperature (**Figure 9a**), however, the regression coefficients for NDVI and precipitation contained both

http://dx.doi.org/10.5772/64740

positive and negative values (**Figure 9b**). It was found that the positive values for NDVI and precipitation were mainly located in Yunnan Province, where the climate is more arid than other areas of the study area. The GWR regression coefficients for dynamic relationships were listed in **Figure 9(c)** and **(d)**. The NDVI was lower with increasing surface temperature, which may be explained as more serious aridity due to the warming. On the other hand, the correlation between the changing rate of NDVI with precipitation were positive, meaning that the increase in NDVI during 1982–2013 could have been caused mainly by the precipitation variations.

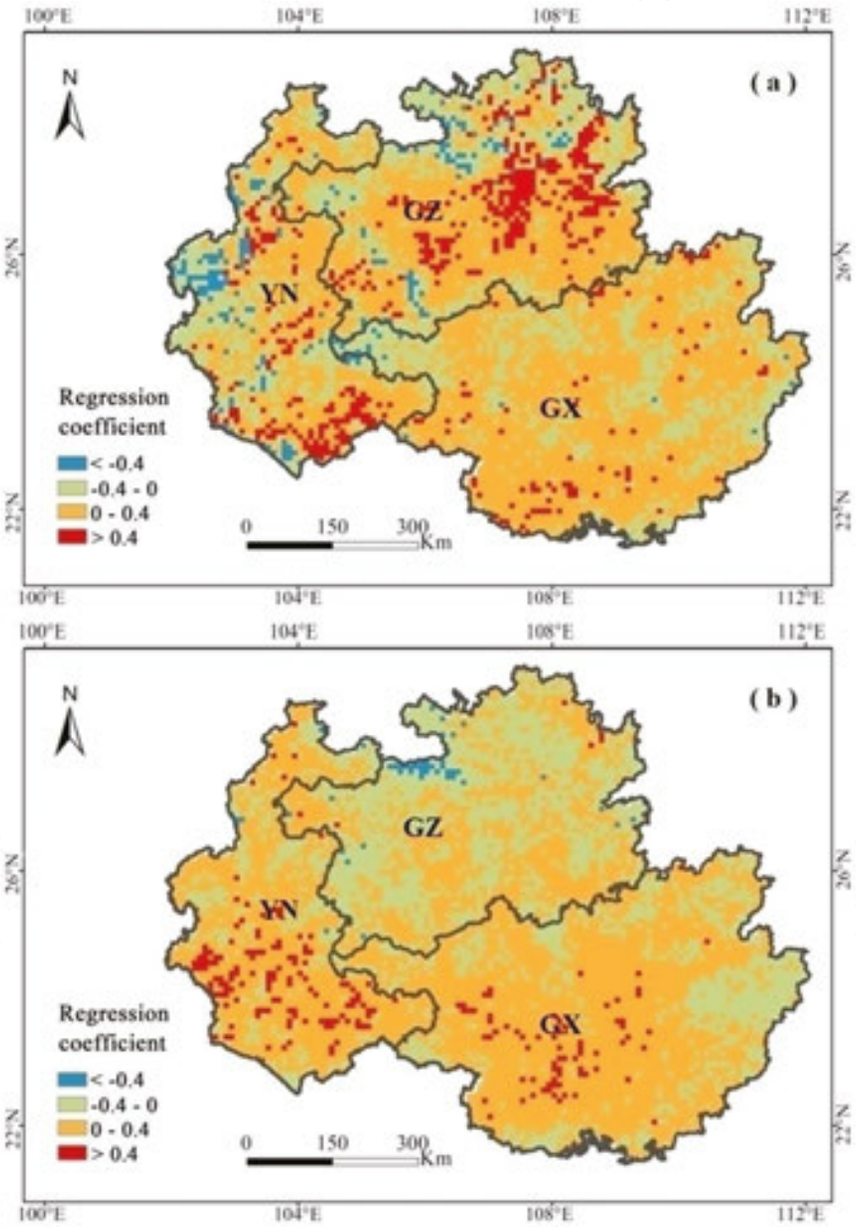

Figure 8. Multivariate regression coefficients of temperature (**a**); and precipitation (**b**) to NDVI based on pixel during 1982–2013.

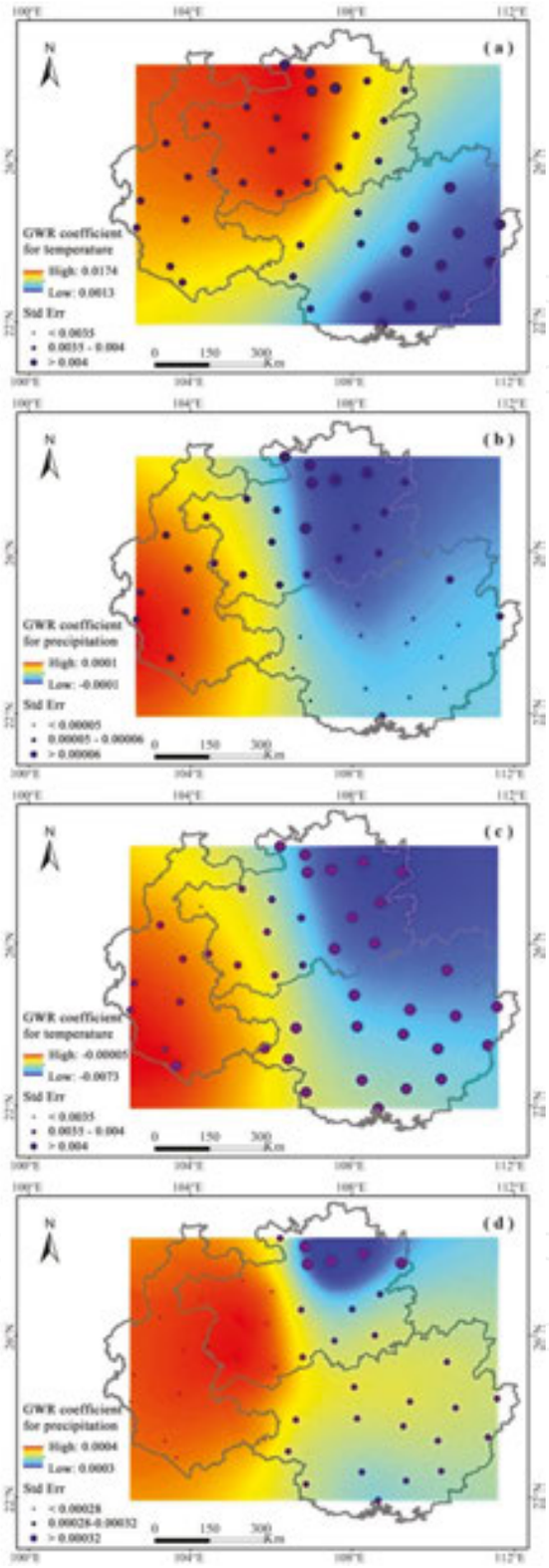

Figure 9. Geographically weighted regression analysis between NDVI and temperature and precipitation during 1982–2013. (**a**) Coefficients image for temperature; (**b**) coefficients image for precipitation; (**c**) coefficients image for temperature trend; (**d**) coefficients image for precipitation trend.

4.3. The decrease in NDVI during 2009–2012 and its climatic explanation

Additional to the uptrend of NDVI from 1982 to 2013, there were some years when the NDVI decreased, that is, from 2009 to 2012. The decreasing rate during this time was −0.017/year. The significant decline was mostly in Guizhou Province where a decreased rate less than −0.02/year was observed (**Figure 10**). Correlation analysis between NDVI and climate change, revealed that the impact of temperature on the decreased NDVI was more profound than that from precipitation (**Figure 11**). Furthermore, the negative relationships between NDVI and precipitation also indicated the indirect impact of precipitation on temperature change. The increase in precipitation with more cloud could have led to the decrease in solar radiation and temperature, thus inhibiting photosynthesis.

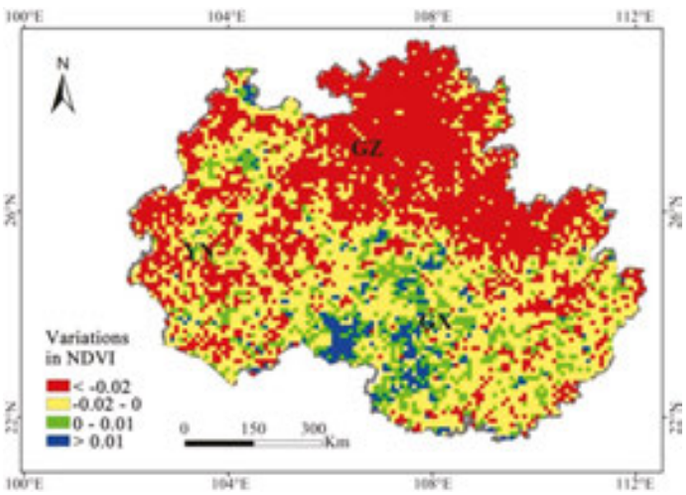

Figure 10. Spatial patterns of variations in growing-season NDVI during 2009–2012.

4.4. Assessing the dynamic downscaling of WRF

Uncertainty on the downscaling capability of regional climate model (RCM) has in most cases led to skepticism for its use. Despite the weakness, the RCM dynamic downscaling is better than the simulations from General Circulation Model (GCM) or reanalysis datasets [13]. Furthermore, the uncertainty increases when the RCM is used to simulate the impact of land cover change on regional climate. In this section, the state-of-the-art RCM's downscaling ability was evaluated first, and was followed by analysis of the climatic effects of land degradation.

To reveal the improvement of WRF simulations over reanalysis dataset, daily rainfall, temperature, and other circulation factors from WRF and reanalysis were compared with the APHROD (Asian Precipitation-Highly-Resolved Observational Data) precipitation dataset, the GTS (Global Telecommunication System) temperature dataset, and the JRA-25 (Japanese 25-year Reanalysis) atmospheric variables dataset. The assessment was conducted from the viewpoint of correlation coefficient (R), bias and root mean square error (RMSE) over the years of 1998, 2000, and 2004 and over 18°–52°N, 86°–136°E (**Table 3**). The lower Bias and RMSE and the higher R values indicate better performance.

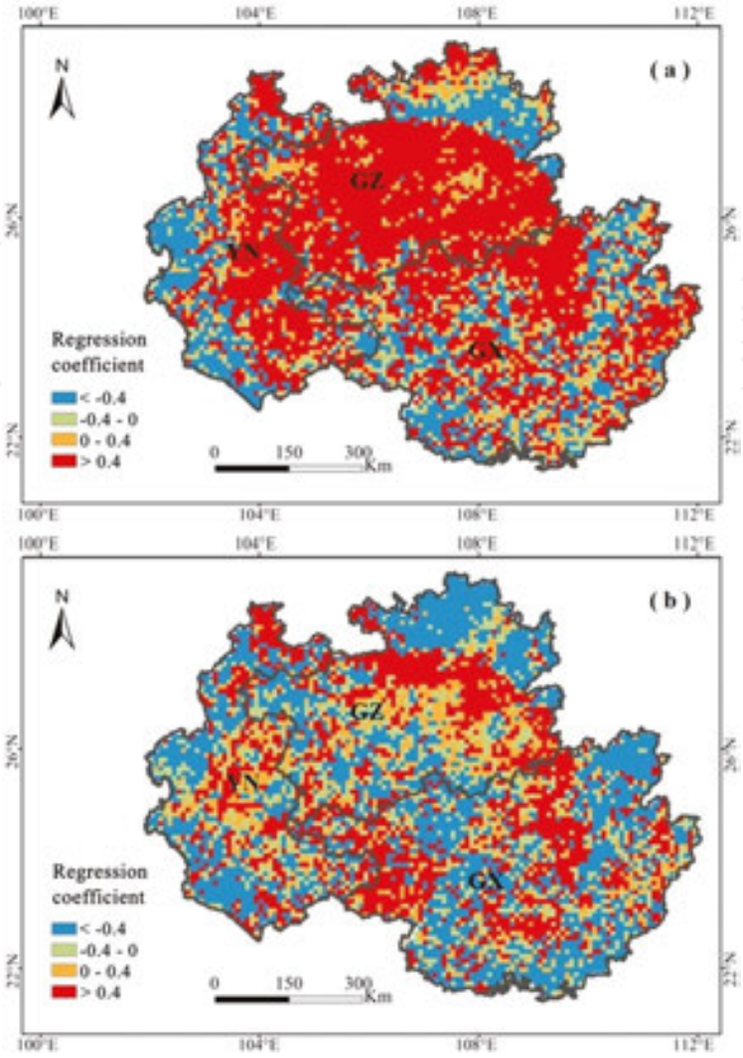

Figure 11. Multivariate regression coefficients of temperature (**a**) and precipitation (**b**) to NDVI based on pixel during 2009–2012.

Variables		Bias	RMSE	R
Precipitation	NCEP R-2	1.95	4.22	0.60
	WRF/SSiB	1.57	3.16	0.78
Temperature	NCEP R-2	−1.93	3.62	0.86
	WRF/SSiB	−2.29	4.21	0.85
VQ700	NCEP R-2	2.89	11.38	0.65
	WRF/SSiB	−1.37	7.49	0.70

VQ700, water vapor flux at 700 hpa (g/kg/ms).

Table 3. Descriptive statistics of ensemble mean JJA daily precipitation, temperature and water vapor flux at 700 hpa from WRF/SSiB and NCEP R-2 over 18°-52°N, 86°-136°E.

http://dx.doi.org/10.5772/64740

We further observed that the phenomenon of most rainfall occurring in the south of China, especially in the south of Yangtze River, can be detected from both WRF simulation and APHROD dataset. From the WRF simulation, there was also an obvious increasing trend from the northwest to southeast in the south of about 38°N with the minimum temperature in Qinghai-Tibetan Plateau. The WRF simulation of precipitation out-performed NCEP R-2, and was probably caused by the improved simulations of low level water vapor flux (**Table 3**), a key factor influencing the atmospheric convection in East Asian summer monsoon. Although the simulated surface temperature from WRF was not improved over NCEP R-2, the clearer spatial information for temperature was presented from WRF output, which suggests that, it is also an applicable tool in downscaling temperature.

4.5. Influence on precipitation and temperature due to KRD

The area over 20°–34°N, 104°–124°E was chosen to investigate the impact of Karst rocky desertification on precipitation and temperature, because the significant and consistent effects were located in this region. There was spatial variation in the precipitation changes among the regions (**Figure 12a**). The reduced rainfall was mainly observed in the middle of Guizhou Karst Plateau. The areas with increased precipitation, mainly the middle and lower parts of Yangtze River and the surrounding areas, were of much larger magnitude and extent than that with decreased rainfall. It can be inferred that the consistent but nonsignificant reduction in rainfall with Guizhou Karst Plateau was due to high moisture influence from the Bay of Bengal. The land surface warming mainly occurred in the areas where the original vegetation types were replaced with bare soil type (**Figure 12b**), while the rainfall changes not only occurred within the desertification area but also beyond the area.

4.6. Influence of KRD on land surface energy balance

As shown in **Figure 13**, the substantial changes of surface energy components occurred in Guizhou Karst Plateau. In the degraded areas, the higher albedo (**Figure 13a**) led to more reflected shortwave radiation from the land surface (**Figure 13b**). Due to the higher surface skin temperature (**Figure 12b**), the outgoing longwave radiation increased significantly, which further caused the reduced net longwave radiation at the surface (**Figure 13c**). Both the reduction of the net shortwave radiation and the net longwave radiation certainly resulted in the decrease in land surface net radiation (**Figure 13d**). More sensible heat flux was also induced by the warmer surface (**Figure 13e**), however, the reduction in surface latent heat flux (**Figure 13f**) was much more than the sensible heat flux increase. The decrease in evaporation was probably contributed by changes in vegetation and soil properties, such as the lower LAI and roughness length, and the higher surface albedo. It can be concluded that evaporation decrease produced the most profound influence on the hydrological balance at land surface. Additionally, the above-mentioned higher temperature in the degraded areas was caused by the reduced evaporative cooling.

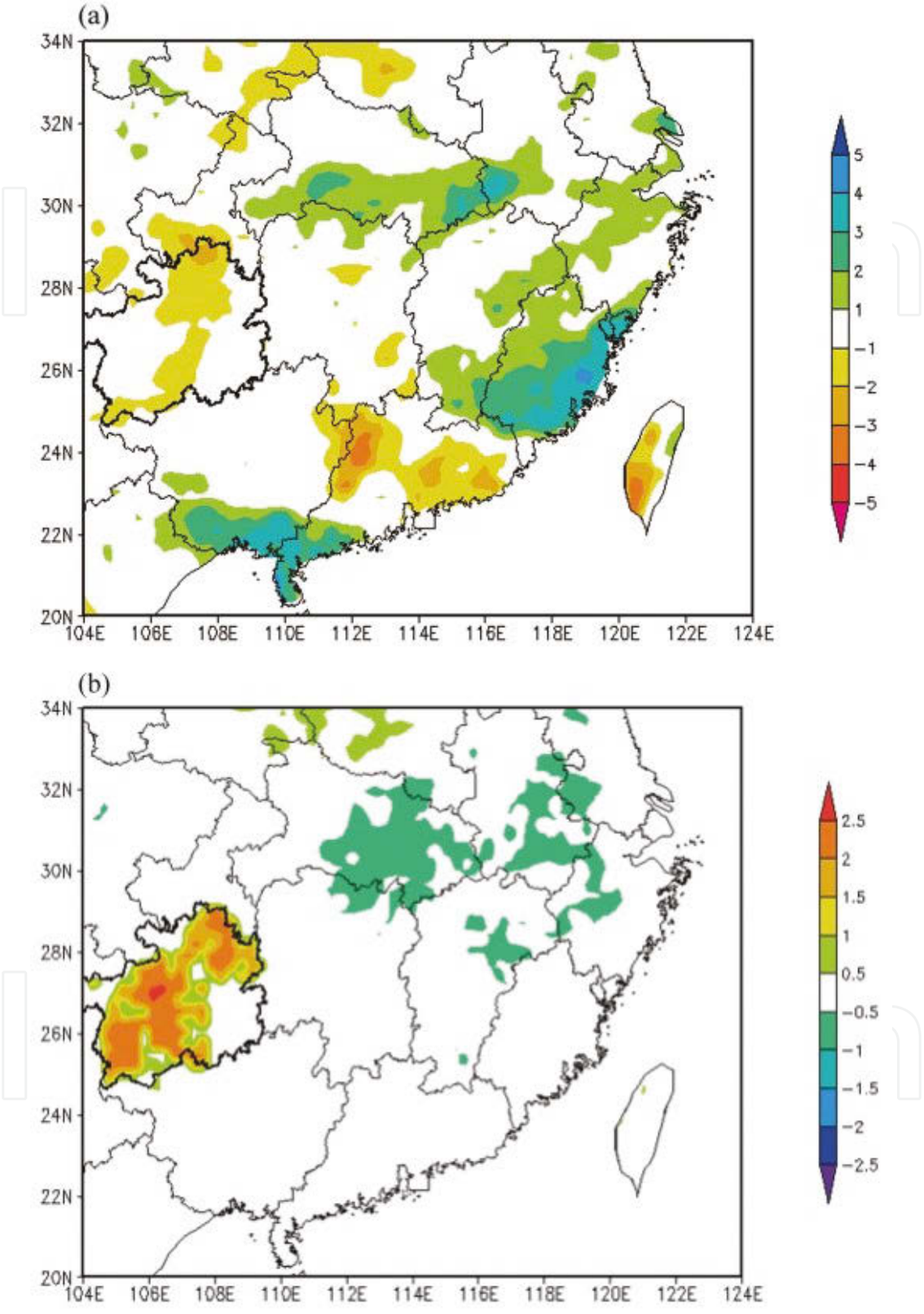

Figure 12. Ensemble mean differences in JJA **(a)** daily precipitation (mm/day) and **(b)** temperature (°C) between Case D and Case C. GKP is bounded by a heavy border.

http://dx.doi.org/10.5772/64740

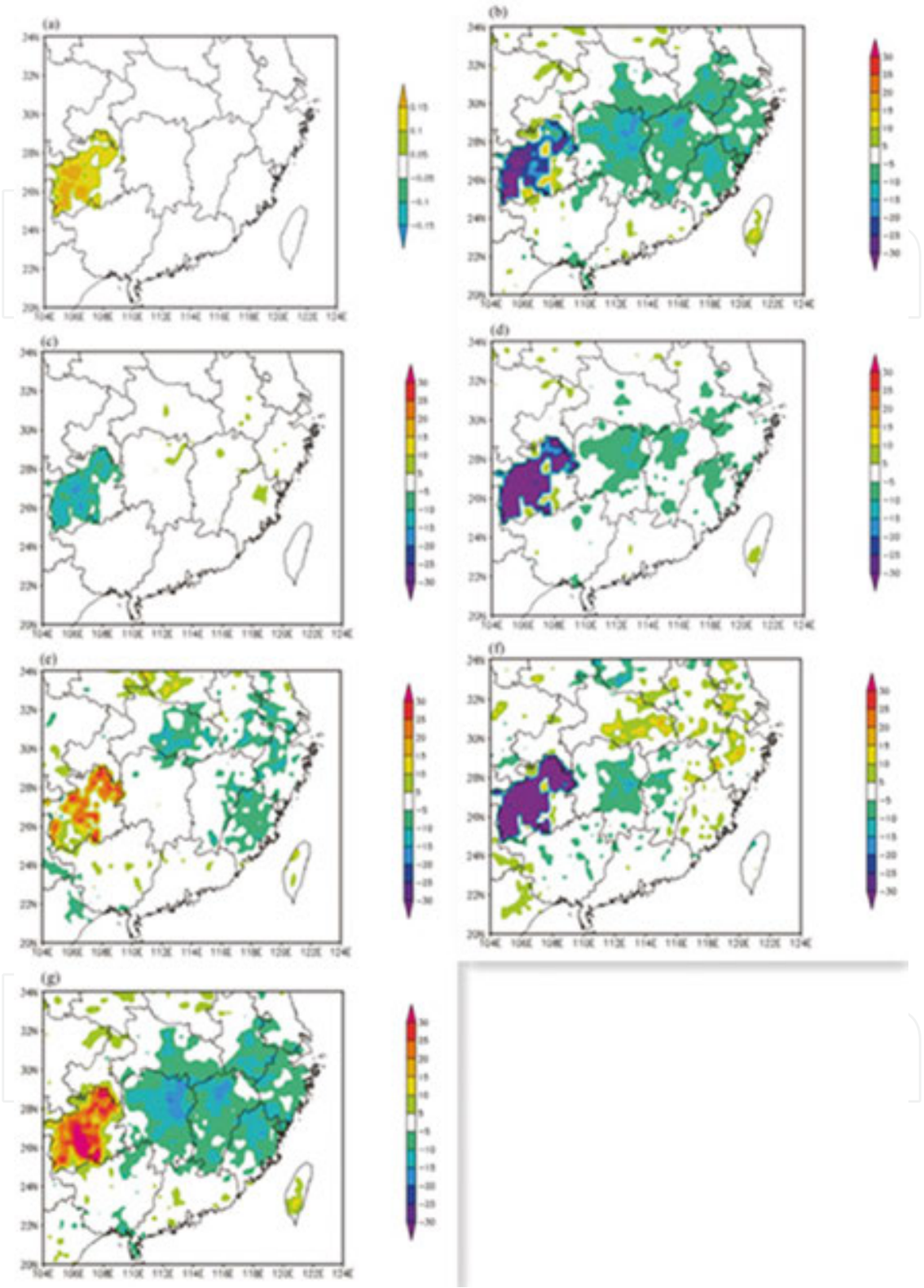

Figure 13. Ensemble mean differences in JJA **(a)** surface albedo, **(b)** net shortwave radiation, **(c)** net longwave radiation, **(d)** net radiation, **(e)** sensible heat flux, **(f)** latent heat flux, and **(g)** incoming shortwave radiation (W/m^2) between Case D and Case C.

Consistent with the spatial changes in precipitation, there were areas with significantly changed energy budget extending beyond the degraded area. Outside the Guizhou Karst Plateau, the variations in sensible heat flux and latent heat flux were controlled by the precipitation differences. For example, in the areas between 30°–34°N, 112°– 120°E (i.e., the southeastern coastal area of China), the increased evaporation (**Figure 13f**) was caused by the increase in precipitation (**Figure 12a**), which further led to the lower temperature (**Figure 12b**), and the lower sensible heat flux (**Figure 13e**). The issue on the impact of atmospheric circulations on precipitation will be discussed in the next section.

Figure 13(g) shows the impacts of cloud albedo and land surface albedo on shortwave radiation. In the degraded areas within Guizhou Karst Plateau, the cloud fraction was reduced due to the less evaporation and moisture flux convergence after land degradation, and the reduced cloud fraction further led to more incoming shortwave radiation. However, the increase in upward shortwave radiation (**Figure 13a**) due to the higher land surface albedo was much more than the downward shortwave radiation, which resulted in the reduced net shortwave radiation (**Figure 13b**). Moreover, in the southeastern coastal areas of China, the increased cloud fractions, consistent with more rainfall, led to the decrease in incoming shortwave radiation, dominating the alteration in net shortwave radiation.

4.7. Effects of KRD on atmospheric circulation

The modified water and energy budget due to Karst rocky desertification was the first-order effects. Because of the different input of heat and moisture into atmospheric circulation, the large-scale circulation features were altered, resulting in climatic effects beyond the desertification area. As shown in **Figure 14**, the weakened 3-month mean wind vector at 700 hPa

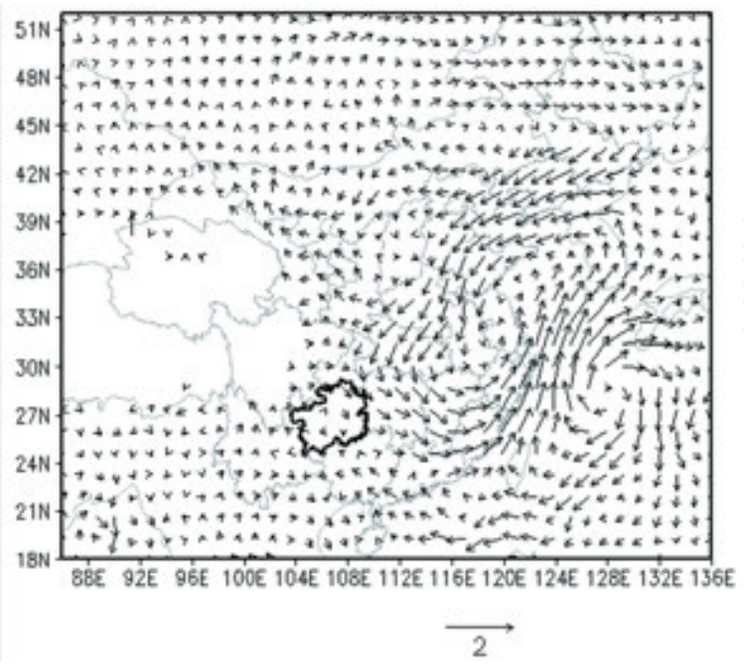

Figure 14. Ensemble mean differences in JJA wind vector (m/s) at 700 hPa between Case D and Case C.

http://dx.doi.org/10.5772/64740

between Case D and Case C was caused by the lower surface heating in GKP (**Figure 13d**). The monsoon airflow from the Bay of Bengal, an important moisture source for the East Asia, was weakened from the degraded areas to the northeast. Furthermore, the weakened southwest airflow had significant impacts on the East Asian monsoon, especially, the anomaly cyclone (**Figure 14**) and the stronger horizontal convergence in the southeastern coastal area that led to the strengthened vertical ascending motion and the increase in precipitation.

On the other hand, the longitude-height section of the composite difference of zonal circulation along 24°–30°N between Case D and Case C was plotted to conduct further analysis (**Figure 15**). After the land degradation in GKP, an anomalous descending motion appeared in both the upper and middle level of troposphere over GKP and the middle and lower troposphere of the adjacent regions to the east. Such circulation modification caused the strengthened ascending motion over 114°–122°E. Moreover, the stronger lifting over the coastal areas led to the increase in the vertically integrated moisture flux convergence (VIMFC) from 1000 to 300 hPa. Consequently, the different circulation and moisture flux reduced the rainfall over GKP and promoted the formation of clouds and the positive rainfall anomalies over southeastern coastal areas of China (**Figure 12a**). Also, in the southeast China, the surface cooling (**Figure 12b**) was induced by the increased amount of clouds and further a negative net cloud radiation forcing.

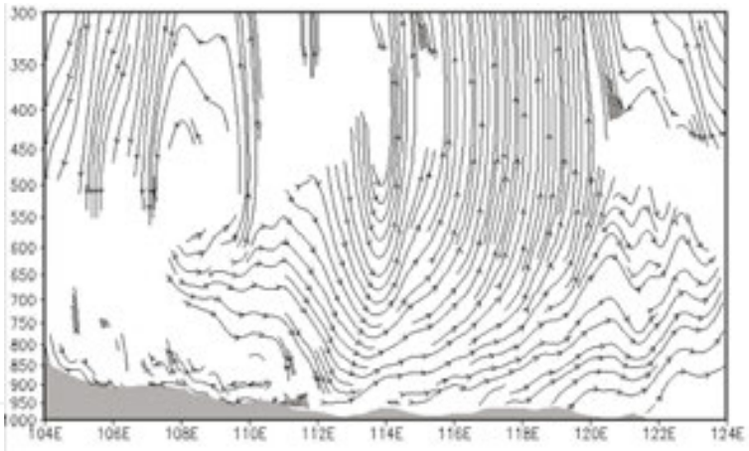

Figure 15. Zonal-height cross sections of ensemble mean differences in JJA zonal (ms^{-1}) and vertical (10–2 ms^{-1}) winds averaged over 24°–30°N. Gray shading indicates topography.

5. Conclusions

The growing-season NDVI increased significantly during the last 30 years in the Karst region of the southwest China. There were also differences in the increase rate of vegetation types. The distribution of NDVI presented obvious spatial patterns, specifically, lower values in the western part and higher values in the east. The correlation between NDVI and climatic factors implied the limiting role of temperature for the vegetation growth and distribution in the study

area, although the regression coefficients presented spatial heterogeneity. Additionally, the decreased NDVI was analyzed to detect the influencing mechanism. It was found that the increased cloud cover and rainfall led to the decrease in solar radiation and temperature, and further impeded photosynthesis.

We also observed that after the land cover change, there is need to consider its climatic effects through the impact of LCC on land surface water and energy budget. Karst rocky desertification (i.e., extensive exposure of basement rocks, serious soil erosion, drastic decrease in soil productivity and appearance of desert-like landscape) can modify the energy budget at land surface and then the regional climate. Specifically, after land degradation, the higher surface albedo and temperature caused the reduced net shortwave radiation and net longwave radiation. The sensible heat flux was increased by the higher temperature. Specifically, the substantial increase in sensible heat flux from ground offset the decrease in that from canopy. Due to higher stomatal resistance and lower LAI, the latent heat flux in KRD was reduced significantly. Less atmospheric heating from degraded land resulted in relative subsidence and less moisture flux convergence (MFC). The decrease in rainfall was probably attributed by both the reduced MFC and the reduced evaporation. A feedback loop was activated when precipitation was affected, for example, the altered soil moisture, vegetation growth, and phenology can further result in less diabatic heating rates, less moisture flux convergence, and lower rainfall. Moreover, the changed rainfall beyond the degraded areas was more significant. The modified energy and water balance due to land degradation weakened the southwest monsoon flow and affected the atmospheric circulation and moisture flux. In the southeastern coastal areas, the precipitation increased due to two reasons: (1) the weaker low-layer anticyclone causing the stronger vertical ascending motion, (2) the air mass diverging in the lower troposphere accompanying rising up over southeastern China.

Acknowledgements

We thank the National Basic Research Program of China (Grant No. 2015CB452702), the National Natural Science Foundation of China (Grant No. 41671098, 41301089), the National Science and Technology Support Program of China (Grant No. 2012BAC19B10, Grant No. 2013BAC04B02) for supporting this work.

Author details

Jiangbo Gao*, Wenjuan Hou, Kewei Jiao and Shaohong Wu

*Address all correspondence to: gaojiangbo@igsnrr.ac.cn

Key Laboratory of Land Surface Pattern and Simulation, Institute of Geographic Sciences and Natural Resources Research, Chinese Academy of Sciences, Beijing, China

References

[1] Parmesan C, Yohe G. A globally coherent fingerprint of climate change impacts across natural systems. Nature. 2003;421:37–42. DOI: 10.1038/nature01286.

[2] Piao SL, Wang XH, Ciais P, Zhu B, Wang T, Liu J. Changes in satellite-derived vegetation growth trend in temperate and boreal Eurasia from 1982 to 2006. Global Change Biology. 2011;17:3228–3239. DOI: 10.1111/j.1365-2486.2011.02419.x.

[3] Beck PSA, Atzberger C, Hogda KA. Improved monitoring of vegetation dynamics at very high latitudes, a new method using MODIS NDVI. Remote Sensing of Environment. 2006;100:321–336. DOI: 10.1016/j.rse.2005.10.021.

[4] Zhao M, Running SW. Drought-induced reduction in global terrestrial net primary production from 2000 through 2009. Science. 2010;329:940–943. DOI: 10.1126/science.1192666.

[5] Piao SL, Ciais P, Huang Y, Shen ZH, Peng SS, Li JS, et al. The impacts of climate change on water resources and agriculture in China. Nature. 2010;467:43–51. DOI: 10.1038/nature09364.

[6] Bounoua L, Defries R, Collatz GJ, Sellers PJ, Khan H. Effects of land cover conversion on surface climate. Climatic Change. 2002;52:29–64. DOI: 10.1023/A:1013051420309.

[7] Pielke RA, Avissar R, Raupach M, Dolman AJ, Xeng Y, Denning S. Interactions between the atmosphere and terrestrial ecosystems: Influence on weather and climate. Global Change. Biology. 1998;4:461–475. DOI: 10.1046/j.1365-2486.1998.t01-1-00176.x.

[8] Huang QH, Cai YL. Spatial pattern of Karst rock desertification in the middle of Guizhou province, southwestern China. Environmental Geology. 2006;52:1325–1330. DOI: 10.1007/s00254-006-0572-y.

[9] Yang QQ, Wang KL, Zhang CH, Yue YM, Tian RC, Fan FD. Spatiotemporal evolution of rocky desertification and its driving forces in Karst areas of northwestern Guangxi, China. Environmental Earth Sciences. 2001;64:383–393. DOI: 10.1007/s12665-010-0861-3.

[10] Xu YQ, Peng J, Shao XM. Assessment of soil erosion using RUSLE and GIS: a case study of the Maotiao River watershed, Guizhou Province, China. Environmental Geology. 2009;56:1643–1652. DOI: 10.1007/s00254-008-1261-9.

[11] Mann HB. Nonparametric tests against trend. Econometrica. 1945;13:245–259. DOI: 10.2307/1907187.

[12] Li Z, Huffman T, McConkey B, Townley-Smith L. Monitoring and modeling spatial and temporal patterns of grassland dynamics using time-series MODIS NDVI with climate and stocking data. Remote Sensing Environment. 2013;138:232–244. DOI: 10.1016/j.rse.2013.07.020.

[13] Gao YH, Xue Y, Peng W, Kang HS, Waliser D. Assessment of dynamic downscaling of the extreme rainfall over East Asia using a regional climate model. Advances in Atmospheric Sciences. 2011;28:1077–1098. DOI: 10.1007/s00376-010-0039-7.

[14] Kanamitsu M, Ebisuzaki W, Woollen J, Yang SK, Hnilo JJ, Fiorino M, Potter GL. NCEP-DOE AMIP-II Reanalysis (R-2). Bulletin of the American Meteorological Society. 2002;83:1631–1643. DOI: 10.1175/BAMS-83-11-1631.

[15] Ren H. A review on the studies of desertification process and restoration mechanism of Karst rocky ecosystem. Tropical Geography. 2005;25:195–200. DOI: 1001-5221(2005)03-0195-06.